PHYSICAL REVIEW E **104**, L063201 (2021)

Letter

Generation of radio frequency radiation by femtosecond filaments

Travis Garrett,[1] Jennifer Elle,[1] Michael White,[1] Remington Reid,[1] Alexander Englesbe,[2] Ryan Phillips,[1]
Peter Mardahl,[1] Erin Thornton,[1] James Wymer,[1] Anna Janicek,[3] Oliver Sale,[3] and Andreas Schmitt-Sody[1]
[1]*Air Force Research Laboratory, Directed Energy Directorate, Albuquerque, New Mexico 87123, USA*
[2]*Naval Research Laboratory, Plasma Physics Division, Washington, DC 20375, USA*
[3]*Leidos Innovations Center, Albuquerque, New Mexico 87106, USA*

(Received 26 February 2021; accepted 17 November 2021; published 15 December 2021)

Recent experiments have shown that femtosecond filamentation plasmas generate ultrabroadband radio frequency radiation (RF). We show that a combination of plasma dynamics is responsible for the RF: A plasma wake field develops behind the laser pulse, and this wake excites (and copropagates with) a surface wave on the plasma column. The surface wave proceeds to detach from the end of the plasma and propagates forward as the RF pulse. We have developed a four-stage model of these plasma wake surface waves and find that it accurately predicts the RF from a wide range of experiments, including both 800-nm and 3.9-μm laser systems.

DOI: 10.1103/PhysRevE.104.L063201

The development of chirped pulse amplification [1] has enabled an array of exotic physics [2–4], including atmospheric filamentation [5]. Filamentation in turn produces interesting and useful effects, from supercontinuum generation [6,7], broadband THz radiation [8,9], and RF pulses, which have recently been explored in great detail [10–15]. We have discovered that a combination of a plasma wake field and a surface wave is responsible for this filament RF. Femtosecond lasers are becoming important spectroscopic tools (both in the laboratory [16] and for remote sensing [17]), and the added production of pulsed RF promises to expand the utility of these systems [18–20], and to provide insight into the physics of filamentation.

During typical $\lambda = 800$ nm filamentation Kerr self-focusing and plasma defocusing are in rough balance, resulting in a plasma column with a density of $n_e \sim 10^{22}$ m^{-3} [21,22]. This electron density corresponds to a plasma frequency of $\omega_{\mathrm{pl}} \simeq 6 \times 10^{12}$ rad/s, which is closely linked to the generation of THz radiation. In the single-color THz theory of Ref. [8] the freshly ionized electrons receive a ponderomotive push from the laser pulse, thus exciting a coherent longitudinal current I_z in the plasma (which is quickly damped by the high collision frequency). This short current pulse translates at c behind the laser pulse, thereby producing a conical shell of radially polarized THz radiation.

The RF resembles the THz radiation in some ways, and differs critically in others. It has a similar conical shell spatial profile and radial polarization, which indicates that a GHz scale longitudinal current pulse is also generated within the plasma. However, it also has a well-defined broadband peak in the 5–15 GHz range (and is not the tail of the THz radiation [11,13,14]) and the RF amplitude grows strongly with decreasing pressure [11,13], in contrast to the THz which falls off sharply [23]. A distinct physical mechanism thus must be responsible for the RF.

Exploratory particle-in-cell (PIC) simulations [24–30] [see Sec. 1 in the Supplemental Material (SM) [31] for more details] provided the key insights that explain the RF generation. They revealed that a hot shell of electrons expands off the plasma surface into the surrounding atmosphere over roughly 50 ps (as anticipated by Ref. [32]), and that the corresponding current density J_r depends strongly on the electron-neutral collision frequency. Subsequent simulations demonstrated that this plasma wake field (PW) excites a surface wave (SW) on the outer boundary of the plasma [namely, a long-wavelength surface plasmon polariton (SPP) [33,34], with a speed approaching c]. Finally, the SW was found to effectively detach from the end of the plasma, with most of the energy being then converted into a broadband RF pulse.

The PWSW numerical model is split into four stages, as length scales spanning seven orders of magnitude need to be resolved. First, the initial electron distribution function $\mathcal{N}_e$ is determined. In a typical $\lambda = 800$ nm experiment a linearly polarized, single-color, 40 mJ pulse is focused into a quartz cell with an $f/60$ mirror, which sets the beam waist ω_0 to 30 μm (10 mJ and $f/15$ focusing are common for $\lambda = 3.9$ μm). The resulting Keldysh parameter $\gamma = \omega_{\mathrm{laser}}\sqrt{2m_e I_{\mathrm{pot}}}/(q_e E)$ is close to 1, so we use the general ionization rate $\mathcal{W}$ from Ref. [35], which is supported by experimental data [36] near atmospheric pressure (other ionization mechanisms will likely be needed for 10-μm lasers [37]). A laser intensity of $I \sim 5 \times 10^{17}$ W/m^2 generates enough plasma at 1 atm for intensity clamping [21] to occur (with $\mathcal{W} \sim 10^{12}$ s^{-1}), which leads to an estimated plasma length L_{pl} of 25 cm, and a radius r_{pl} of $\sim$1 mm (see Sec. 2 of SM [31] for more details). At 1 Torr I increases to $\sim 2 \times 10^{18}$ W/m^2, which ionizes much of the O$_2$, and the plasma is reduced to $L_{\mathrm{pl}} \simeq 13$ cm and $r_{\mathrm{pl}} \simeq 0.5$ mm. In turn, the lower-energy 3.9-μm laser plasmas are shorter, with L_{pl} ranging from about 1 to 2 cm.

These estimates match well (within 25%) with photographic measurements of the plasma taken at different pressures (available in Sec. 2 of SM [31]). Simulations of filamentation with these parameters have also been performed using a unidirectional pulse propagation equations (UPPE)

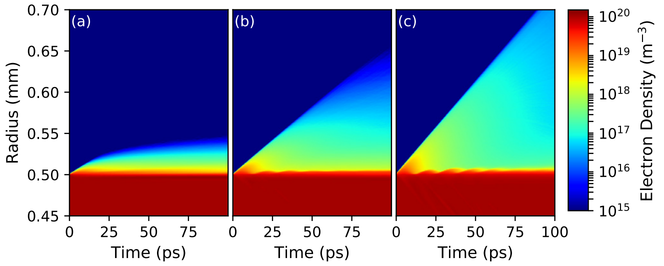

FIG. 1. Log plots of the electron density $n_e(r, t)$ showing the plasma wake variation at pressures of (a) 100, (b) 10, and (c) 1 Torr for a $\lambda = 800$ nm laser pulse. The plasma outer radius has been set to $r_{\rm pl} = 0.5$ mm for all three pressures for comparison purposes.

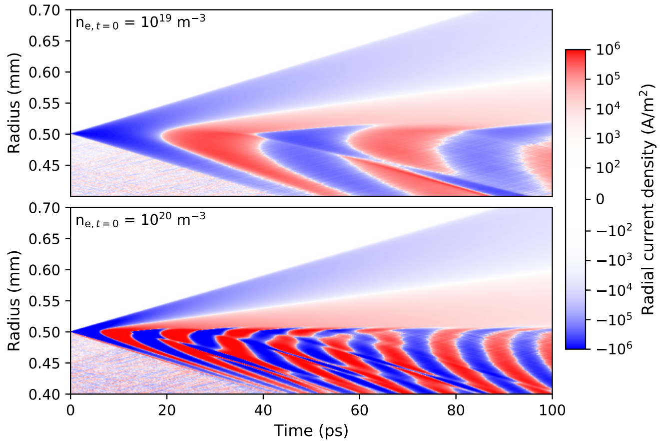

FIG. 2. Log plots of the radial current density $J_r(r, t)$ at 1 Torr (800-nm source), as it evolves in a transverse slice of plasma. The initial density at the edge of the plasma has been given a step function profile, with a value of $n_e = 10^{19}$ m^{-3} in the top plot and $n_e = 10^{20}$ m^{-3} on the bottom. The profiles of the plasma wakes outside the column ($r > r_{\rm pl} = 0.5$ mm) are quite similar, while at the surface SPPs are excited at roughly ∼20 and ∼60 GHz, respectively, along with higher-frequency volume plasmons in the interior.

solver [38]. These agree with the overall dimensions of the plasma column, but also indicate that there is rich fine-scale structure throughout the plasma (as expected as we are in the multifilamentary regime [39–41]). For this Letter we simplify and do not include fine-scale plasma perturbations. The plasma column is approximated as having a constant density central core due to intensity clamping, and then a 100 μm radial ramp down to zero density at the outer radius $r_{\rm pl}$.

The velocity distribution is determined by our PIC code: Given $E(\vec{x}, t)$ the air is ionized at the $\mathcal{W}$ rate [35] and the new electrons are accelerated through the remainder of the pulse [28] (code to perform these calculations is included in SM [31]). In general, the velocity distribution is influenced by both the details of strong field ionization near $\gamma = 1$ (e.g., Ref. [42]), and by the deformation of the laser pulse during filamentation. For this work we further simplify and assume that the electrons are ionized with zero initial velocity and are then accelerated by the remainder of a Gaussian pulse (with $\hat{x}$ polarization and propagating in $+z$). As a whole the initial $\mathcal{N}_e$ is highly non-Maxwellian, and at 100 Torr has a peak kinetic energy $K_{\rm tail} \simeq 5$ eV, and an average kinetic energy $K_{\rm avg} \simeq 0.6$ eV, while these increase at 1 Torr to $K_{\rm tail} \simeq 16$ eV and $K_{\rm avg} \simeq 2$ eV. For 3.9-μm lasers the kinetic energy is ∼25 times larger, as the laser intensities are comparable and the energy scales as λ^2.

We next consider the evolution of the plasma column. We construct thin transverse slices of plasma given $\mathcal{N}_e$, with periodic boundary conditions used in the longitudinal direction $\hat{z}$ (which is valid to leading order as the electron velocities are a small fraction of c) and simulate the radial evolution with our PIC code. The Debye length is quite small, $\lambda_{\rm Debye} \simeq 10$ nm, so we use an energy conserving method [43] to calculate the Lorentz force. The electron-neutral elastic collision frequency ν_{eN} depends on the cross sections for O_2 and N_2, which for our energies is roughly 10 Å^2 [44]. In turn, the electron-ion momentum-transfer collision frequency is given by $\nu_{ei} = 7.7\times10^{-12} n_e \ln(\Lambda_C)/K_{eV}^{3/2}$, where $\Lambda_C = 6\pi n_e \lambda_{\rm Debye}^3$ [45]. The resulting radial current density J_r and electron density n_e are then recorded as functions of radius and time (more details can be found in Sec. 3 of SM [31]). These are well resolved with a mesh resolution of $\Delta x = \Delta y = 2$ μm, and a macroparticle weight of ∼10 on the outer edge of the plasma.

The electron number density for $\lambda = 800$ nm simulations of the PW at 100, 10, and 1 Torr can be seen in Fig. 1. The outer edge of the plasma at $t = 0$ has a simplified step function profile, with $n_e = 10^{20}$ m^{-3} at radius $r_{\rm pl} = 0.5$ mm. Thus, in addition to the PW being launched off of the edge of this plasma, a coherent radial plasma frequency oscillation of ∼90 GHz is stimulated in the interior [46] and a SPP at ∼63 GHz is excited on the surface [33,34,47]. The PW that expands out into the neutral atmosphere ($r > r_{\rm pl}$) is insensitive to the density of the outer edge of the plasma (see Fig. 2), as opposed to the excited surface and volume plasmons.

Analytic approximations provide a useful complement to the simulations. Consider the late-time electron density at a small distance r_Δ off the surface of the plasma at radius $r_{\rm pl}$. Using Gauss's law and approximating $\ln[(r_{\rm pl} + r_\Delta)/r_{\rm pl}]$ as $r_\Delta/r_{\rm pl}$ for $r_\Delta \ll r_{\rm pl}$, we find that the number of electrons per unit length n_L that escape to r_Δ scales as

$$n_L(r_\Delta) \simeq \frac{2\pi\epsilon_0 K_{eV}}{q_e}\frac{r_{\rm pl}}{r_\Delta}, \tag{1}$$

where $K_{eV} \simeq K_{\rm tail}$ is the kinetic energy of the hot electrons that lead the escape. The radial electrostatic field $E_{r,\rm stat}$ that corresponds to n_L has a simple form: $E_{r,\rm stat}(r_\Delta) = K_{eV}/r_\Delta$. At $\lambda = 800$ nm and 1 Torr, $K_{\rm tail} \simeq 16$ eV and $r_\Delta \simeq 60$ μm, giving $E_{r,\rm stat} \simeq 2.7 \times 10^5$ V/m. This allows for an estimate of the PW evolution timescale: An electron with energy $K_{\rm tail} = 16$ eV in an electric field of this magnitude follows a parabolic trajectory over 100 ps. This compares well with the spread of electrons seen in Fig. 1. The magnitude of the radial current density can likewise be approximated as

$$J_r \simeq v_{\rm eff}(t)\frac{q_e n_L}{2\pi r_{\rm pl} r_\Delta}, \quad v_{\rm eff}(t) = \min\begin{cases} v_{\rm tail}, \\ v_{\rm diff}(t), \end{cases} \tag{2}$$

where the effective velocity $v_{\rm eff}(t)$ is the minimum of the tail velocity and the Fickian diffusion speed $v_{\rm diff}(t) = [K_{\rm tail}/(m_e \nu t)]^{1/2}$. At 1 Torr this gives $J_r \simeq 1 \times 10^5$ A/m^2. Finally we note that caution is needed for small r_Δ values:

Eqs. (1) and (2) only hold up to densities that are comparable to the original plasma edge density.

We next switch from these transverse PIC simulations to a continuum finite-difference time-domain (FDTD)-Drude model in a two-dimensional (2D) axisymmetric coordinate system [26] that spans the length of the plasma. The Drude model $\partial_t \vec{J}_{\rm pl} + \nu_{\rm pl}\vec{J}_{\rm pl} = \epsilon_0\omega_{\rm pl}^2\vec{E}$ is integrated into the code via an auxiliary differential equation [48]. A mixed resolution of $\Delta r = 2\ \mu$m and $\Delta z = 50\ \mu$m suffices to resolve the SWs. The PW current profile J_r is driven across the surface of the plasma column in the longitudinal direction at the speed of light. In this work only the external radial currents $J_{r>r_{\rm pl}}$ are used to drive the SW and subsequent RF (see Sec. 4 of SM [31] for more details). The higher-frequency volume plasmons can also excite waves in the neighboring lower-density plasma, but we suspect that including a fine-scale plasma structure will act as the surface roughness [49] and cause these to continuously detach.

As expected, the PW current excites a broadband surface wave with similar frequency content. The frequency ω of the wave is considerably lower than the limit SPP frequency and it thus travels at velocity $c[(2\omega^2 - \omega_{\rm pl}^2)/(\omega^2 - \omega_{\rm pl}^2)]^{1/2}$ which approaches the speed of light. The resulting phase-matched copropagation leads to a steady growth in the surface wave intensity (see also Refs. [50,51]).

The SW is well approximated by the Sommerfeld-Goubau [52,53] solution for SPPs on a cylinder of finite conductivity. The external radial component of the electric field E_r has the form

$$E_r(r, z, t) = -\frac{\pi r_{\rm pl} E_0}{2r_{\rm outer}} e^{i(\omega t - hz)} H_1^{(1)}\left(r\sqrt{k^2 - h^2}\right), \tag{3}$$

for waves of frequency ω propagating in the $+z$ direction, with an amplitude of E_0 at the surface. The complex h wave number describes the SW wavelength and attenuation length scale, k is the free-space wave number $k = \omega/c$, $H_1^{(1)}$ is a Hankel function of the first kind with order 1, and $r_{\rm outer} = 1/|\sqrt{k^2 - h^2}|$. For radii $r_{\rm pl} < r < r_{\rm outer}$ the Hankel function with a complex argument is approximately $H_1^{(1)} \simeq -2r_{\rm outer}/(\pi r)$, and for larger radii it falls off exponentially (as is typical for SPPs).

Recent work [54,55] has simplified the calculation of h through the use of the Lambert W function. Given a typical plasma conductivity σ, a complex ξ can be defined,

$$\xi = -\frac{k e^{-2\gamma_{\rm euler}}}{2}\sqrt{\frac{\epsilon_0\omega}{2\sigma}}\, r_{\rm pl}(1 + i) \tag{4}$$

(where $\gamma_{\rm euler}$ is the Euler-Mascheroni constant), and h is then given by

$$h = \sqrt{k^2 + \frac{4\xi e^{-2\gamma_{\rm euler}}}{r_{\rm pl}^2 W_1(\xi)}}, \tag{5}$$

where the first branch of W is used. At 1 Torr the plasma has a radius $r_{\rm pl} \simeq 0.5$ mm and conductivity $\sigma \simeq 2 \times 10^3$ S/m, and thus for a 10-GHz SW we find $h \simeq 210 + 3.2i$. The dispersive SW thus travels at about $0.988c$, attenuates by a factor of $1/e$ every 30 cm (if not being actively excited), and has a $1/r$ transverse envelope out to $r_{\rm outer} \simeq 2.4$ cm, all of which compares well with simulations.

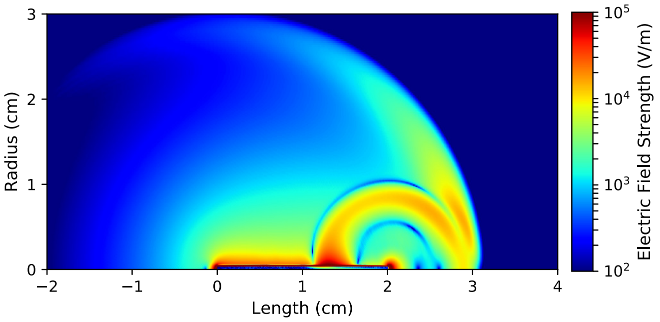

FIG. 3. Log plot of electric field strength shortly after the detachment of a $\lambda = 3.9\ \mu$m, 10-Torr surface wave from a 2-cm plasma column, as simulated by the axisymmetric FDTD-Drude model.

We next consider the excitation of the surface wave by the plasma wake currents. An isolated Hertzian dipole with uniform current I along an antenna of length L will radiate electromagnetic waves at a wavelength $\lambda_{\rm Dipole}$ with power $P_{\rm Dipole} = (\pi\eta_0/3)I^2L^2/\lambda_{\rm Dipole}^2$. In our case we have a radial current distribution of approximate length r_Δ that is normal to a conducting cylinder of radius $r_{\rm pl}$. When there is a separation of length scales $r_\Delta \ll r_{\rm pl} \ll \lambda_{\rm SW}$ and an overall radial current of I_r, then the power that is primarily radiated into SWs is

$$P_{\rm SW} \simeq \frac{\pi\eta_0}{60} I_r^2 \frac{r_\Delta^2}{r_{\rm pl}^{5/3}\lambda_{\rm SW}^{1/3}} \tag{6}$$

[where we have simplified with $\lambda_{\rm SW} = 2\pi/{\rm Re}(h)$]. We note that the dimensionless term $r_\Delta^2/(r_{\rm pl}^{5/3}\lambda_{\rm SW}^{1/3})$ (compare to $L^2/\lambda_{\rm Dipole}^2$ for the Hertzian dipole) has different asymptotic scalings in other length-scale regimes. Equation (6) applies both to a stationary radial antenna and the $\pm z$ wave trains it emits, and to our case, where the antenna translates at c with its comoving SW pulse.

The total effective current $I_r(z)$ is found by integrating the current density J_r from 0 to z, and absent dissipation the amplitude E_0 of the SW in (3) would grow linearly (for constant J_r). However, there is dissipation due to the finite conductivity of the plasma, and the attenuation coefficient $\alpha = {\rm Im}(h)$ is similar in magnitude to $1/L_{\rm pl}$. The SW thus grows linearly initially and then saturates after several $1/\alpha$, and the effective

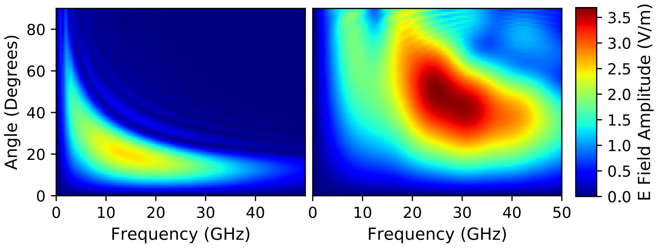

FIG. 4. Plots of simulated electric field strength as a function of frequency and angle for RF pulses from a 40-mJ, $f_N = 60$, 800-nm laser source (left [11]) and a 12-mJ, $f_N = 15$, 3.9-μm source (right [13]), with both cases run at 10 Torr. The numerical profiles and amplitudes closely match the experimental results.

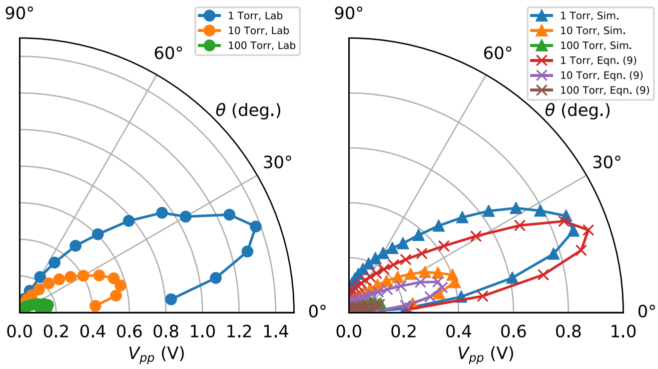

FIG. 5. Polar plots of the detector peak-to-peak voltage V_{pp} for the $\lambda = 800$ nm laser source as a function of angle and pressure as measured in the laboratory (left), and as calculated by both the simulation framework (right, triangles), and by the associated analytic approximations (right, × ticks) that culminate in (9).

total radial current after propagating a distance z is

$$I_r(z) = 2\pi r_{\rm pl} J_r \frac{1 - e^{-\alpha z}}{\alpha}. \tag{7}$$

We express the amplitude of the final SW in terms of its longitudinal current as $I_z = 2\pi r_{\rm pl} E_0/\eta_0$. Integrating (3) to find the SW peak power and setting this equal to (6) we find

$$I_z(z) = \frac{2\pi^2 r_\Delta J_r (1 - e^{-\alpha z})}{\alpha[30 \ln(r_{\rm outer}/r_{\rm pl})]^{1/2}} \left(\frac{r_{\rm pl}}{\lambda_{\rm SW}}\right)^{1/6}. \tag{8}$$

For the $\lambda = 800$ nm laser this gives $I_z \simeq 0.6$ A at the end of the plasma at 1 Torr, a current of $I_z \simeq 0.2$ A at 10 Torr, and $I_z \simeq 0.05$ A at 100 Torr, which are close to the measured currents in the corresponding simulations.

When the surface wave reaches the end of plasma the majority of the energy detaches and propagates forward as the RF pulse, with the reflected wave decaying as it travels back down the plasma. Figure 3 shows an example of this, where the SW has just detached from a 2-cm plasma column produced by a $\lambda = 3.9$ μm laser source at 10 Torr. In this way the system resembles a surface wave end-fire antenna [56,57]. The second half of the primarily one-cycle RF pulse forms as the SW separates from the plasma, with some variation in the profile dependent on the abruptness of the detachment. The recorded $I_z(z, t)$ currents from the SW simulation are used in a $\sim$1 m^2 laboratory scale axisymmetric FDTD model, with resolution $\Delta r = \Delta z = 0.5$ mm. Plots of the resulting Fourier transformed RF field strengths at 10 Torr for both $\lambda = 800$ nm and $\lambda = 3.9$ μm simulations can be seen in Fig. 4 (see Sec. 5 of SM [31] for more details).

To directly compare with laboratory results the simulated electric fields are converted to peak-to-peak voltages V_{pp} via a frequency-dependent calibration factor $C_{E/V}(f_{\rm GHz}) \simeq 50 + 10 f_{\rm GHz}$ (which captures the horn antenna response [11]). We adapt an equation for energy spectral density radiated per unit solid angle derived for THz radiation [8],

$$\frac{d^2U}{d\omega d\Omega} = \frac{|I_z(\omega)|^2 \sin^2\theta}{4\pi\epsilon_0 c(1 - \cos\theta)^2} \sin^2\left(\frac{L_{pl}\omega}{2c}(1 - \cos\theta)\right), \tag{9}$$

to construct voltage profiles for our analytic approximations. The average amplitude of I_z (8) over the length of the plasma is applied to a $\sim$10 GHz pulse, which is Fourier transformed for use with (9) (along with the calibration factor), and then converted back to an effective V_{pp} (code that implements all of these analytic approximations is available in SM [31]).

In general, simulations with varying pressures, focal geometries, and laser pulse energies and wavelengths all produce RF that nicely matches recent experimental results [11–14]. The magnitude of the simulated RF is a bit lower than the laboratory data for the runs shown in Fig. 5, but is within the errors for both the simulations and in the experimental data. Subtle changes in Ti:sapphire laser alignment generates ±50% amplitude variations at a given pressure (with the spatial and frequency content being much more stable). It is suspected that the slight laser pulse variations are amplified during filamentation, leading to fine-scale changes in the plasma radius, density, and electron velocities. Plausible variations in the same parameters lead to comparable changes in the simulated RF amplitude as well.

We have demonstrated that a plasma wake field that excites a surface wave is responsible for the generation of filament RF. The rich internal dynamics of the plasma merits further research: We expect that stochastic higher-frequency RF may inform on the fine-scale structure of the plasma and the nonlinear optics that generate it. The ionization model needs to be expanded to include more physical effects (e.g., Refs. [37,42,58]), and strong field ionization can be further explored with noble gas filament RF. The plasma can also be driven into the strongly coupled regime with harder focusing, and we intend to model resulting RF with the use of Refs. [59,60]. Finally, we note that it may be possible to recreate the core mechanism—an antenna that copropagates with the wave that it excites—in other settings and thereby drive strong coherent radiation.

Acknowledgments. The authors thank Edward Ruden, Serge Kalmykov, and Charles Armstrong for useful discussions, and the Air Force Office of Scientific Research (AFOSR) for support via Laboratory Tasks No. FA9550-18RDCOR0009 and No. FA9550-19RDCOR027. This work was supported in part by high-performance computer time and resources from the DoD High Performance Computing Modernization Program. This work is approved for public release; distribution is unlimited (Public Affairs release approval No. AFRL-2020-0489).

[1] D. Strickland and G. Mourou, Compression of amplified chirped optical pulses, Opt. Commun. **56**, 219 (1985).

[2] J. Faure, Y. Glinec, A. Pukhov, S. Kiselev, S. Gordienko, E. Lefebvre, J.-P. Rousseau, F. Burgy, and V. Malka, A laser–plasma accelerator producing monoenergetic electron beams, Nature (London) **431**, 541 (2004).

[3] X. Liu, D. Du, and G. Mourou, Laser ablation and micromachining with ultrashort laser pulses, IEEE J. Quantum Electron. **33**, 1706 (1997).

[4] A. Di Piazza, C. Müller, K. Z. Hatsagortsyan, and Ch. H. Keitel, Extremely high-intensity laser interactions with fundamental quantum systems, Rev. Mod. Phys. **84**, 1177 (2012).

[5] A. Braun, G. Korn, X. Liu, D. Du, J. Squier, and G. Mourou, Self-channeling of high-peak-power femtosecond laser pulses in air, Opt. Lett. **20**, 73 (1995).

[6] A. Brodeur and S. L. Chin, Ultrafast white-light continuum generation and self-focusing in transparent condensed media, J. Opt. Soc. Am. B **16**, 637 (1999).

[7] V. P. Kandidov, O. G. Kosareva, I. S. Golubtsov, W. Liu, A. Becker, N. Akozbek, C. M. Bowden, and S. L. Chin, Self-transformation of a powerful femtosecond laser pulse into a white-light laser pulse in bulk optical media (or supercontinuum generation), Appl. Phys. B **77**, 149 (2003).

[8] C. D. Amico, A. Houard, S. Akturk, Y. Liu, J. Le Bloas, M. Franco, B. Prade, A. Couairon, V. T. Tikhonchuk, and A. Mysyrowicz, Forward THz radiation emission by femtosecond filamentation in gases: Theory and experiment, New J. Phys. **10**, 013015 (2008).

[9] V. A. Andreeva, O. G. Kosareva, N. A. Panov, D. E. Shipilo, P. M. Solyankin, M. N. Esaulkov, P. G. de Alaiza Martínez, A. P. Shkurinov, V. A. Makarov, L. Bergé *et al.*, Ultrabroad Terahertz Spectrum Generation from an Air-Based Filament Plasma, Phys. Rev. Lett. **116**, 063902 (2016).

[10] B. Forestier, A. Houard, M. Durand, Y.-B. André, B. Prade, J.-Y. Dauvignac, F. Perret, Ch. Pichot, M. Pellet, and A. Mysyrowicz, Radiofrequency conical emission from femtosecond filaments in air, Appl. Phys. Lett. **96**, 141111 (2010).

[11] A. Englesbe, J. Elle, R. Reid, A. Lucero, H. Pohle, M. Domonkos, S. Kalmykov, K. Krushelnick, and A. Schmitt-Sody, Gas pressure dependence of microwave pulses generated by laser-produced filament plasmas, Opt. Lett. **43**, 4953 (2018).

[12] A. Janicek, E. Thornton, T. Garrett, A. Englesbe, J. Elle, and A. Schmitt-Sody, Length dependence on broadband microwave emission from laser-generated plasmas, IEEE Trans. Plasma Sci. **48**, 1979 (2020).

[13] A. V. Mitrofanov, D. A. Sidorov-Biryukov, M. M. Nazarov, A. A. Voronin, M. V. Rozhko, A. B. Fedotov, and A. M. Zheltikov, Coherently enhanced microwave pulses from midinfrared-driven laser plasmas, Opt. Lett. **46**, 1081 (2021).

[14] A. Englesbe, J. Elle, R. Schwartz, T. Garrett, D. Woodbury, D. Jang, K.Y. Kim, H. Milchberg, R. Reid, A. Lucero, D. Gordon, R. Phillips, S. Kalmykov, and A. Schmitt-Sody, Ultrabroadband microwave radiation from near-and mid-infrared laser-produced plasmas in air, Phys. Rev. A **104**, 013107 (2021).

[15] A. V. Mitrofanov, A. A. Voronin, M. V. Rozhko, D. A. Sidorov-Biryukov, M. M. Nazarov, A. B. Fedotov, and A. M. Zheltikov, Polarization and spatial mode structure of mid-infrared-driven terahertz-to-microwave radiation, ACS Photonics **8**, 1988 (2021).

[16] T. Kampfrath, K. Tanaka, and K. A. Nelson, Resonant and nonresonant control over matter and light by intense terahertz transients, Nat. Photonics **7**, 680 (2013).

[17] T. A. Labutin, V. N. Lednev, A. A. Ilyin, and A. M. Popov, Femtosecond laser-induced breakdown spectroscopy, J. Anal. At. Spectrom. **31**, 90 (2016).

[18] G. B. Park and R. W. Field, Perspective: The first ten years of broadband chirped pulse Fourier transform microwave spectroscopy, J. Chem. Phys. **144**, 200901 (2016).

[19] A. Doll, S. Pribitzer, R. Tschaggelar, and G. Jeschke, Adiabatic and fast passage ultra-wideband inversion in pulsed EPR, J. Magn. Reson. **230**, 27 (2013).

[20] J. Capmany and D. Novak, Microwave photonics combines two worlds, Nat. Photonics **1**, 319 (2007).

[21] A. Couairon and A. Mysyrowicz, Femtosecond filamentation in transparent media, Phys. Rep. **441**, 47 (2007).

[22] S. L. Chin, *Femtosecond Laser Filamentation*, Vol. 55 (Springer, Berlin, 2010).

[23] G. Rodriguez and G. L. Dakovski, Scaling behavior of ultrafast two-color terahertz generation in plasma gas targets: Energy and pressure dependence, Opt. Express **18**, 15130 (2010).

[24] C. K. Birdsall and A. B. Langdon, *Plasma Physics via Computer Simulation* (CRC Press, Boca Raton, FL, 2004).

[25] R. E. Peterkin and J. W. Luginsland, A virtual prototyping environment for directed-energy concepts, Comput. Sci. Eng. **4**, 42 (2002).

[26] A. Taflove and S. C. Hagness, *Computational Electrodynamics: The Finite-Difference Time-Domain Method* (Artech House, London, 2005).

[27] K. Yee, Numerical solution of initial boundary value problems involving Maxwell's equations in isotropic media, IEEE Trans. Antennas Propag. **14**, 302 (1966).

[28] J. P. Boris, Relativistic plasma simulation-optimization of a hybrid code, in *Proceedings of the Fourth Conference on Numerical Simulation of Plasmas*, edited by J. P. Boris and R. A. Shanny (U.S. Government Printing Office, Washington, D.C., 1970), pp. 3–67.

[29] J. Villasenor and O. Buneman, Rigorous charge conservation for local electromagnetic field solvers, Comput. Phys. Commun. **69**, 306 (1992).

[30] J.-P. Berenger, A perfectly matched layer for the absorption of electromagnetic waves, J. Comput. Phys. **114**, 185 (1994).

[31] See Supplemental Material at http://link.aps.org/supplemental/10.1103/PhysRevE.104.L063201 for details on the numerical methods used in this Letter, along with the code that implements the analytic approximations, and simulation movies.

[32] B. Zhou, A. Houard, Y. Liu, B. Prade, A. Mysyrowicz, A. Couairon, P. Mora, C. Smeenk, L. Arissian, and P. Corkum, Measurement and Control of Plasma Oscillations in Femtosecond Filaments, Phys. Rev. Lett. **106**, 255002 (2011).

[33] J. M. Pitarke, V. M. Silkin, E. V. Chulkov, and P. M. Echenique, Theory of surface plasmons and surface-plasmon polaritons, Rep. Prog. Phys. **70**, 1 (2006).

[34] S. A. Maier, S. R. Andrews, L. Martin-Moreno, and F. J. Garcia-Vidal, Terahertz Surface Plasmon-Polariton Propagation and Focusing on Periodically Corrugated Metal Wires, Phys. Rev. Lett. **97**, 176805 (2006).

[35] S. V. Popruzhenko, V. D. Mur, V. S. Popov, and D. Bauer, Strong Field Ionization Rate for Arbitrary Laser Frequencies, Phys. Rev. Lett. **101**, 193003 (2008).

[36] A. Sharma, M. N. Slipchenko, M. N. Shneider, X. Wang, K. A. Rahman, and A. Shashurin, Measurements of electron numbers in femtosecond laser induced plasmas using Rayleigh microwave scattering, in *2018 AIAA Aerospace Sciences Meeting* (AIAA, Reston, VA, 2018), p. 0177.

[37] S. Tochitsky, E. Welch, M. Polyanskiy, I. Pogorelsky, P. Panagiotopoulos, M. Kolesik, E. M. Wright, S. W. Koch, J. V. Moloney, J. Pigeon *et al.*, Megafilament in air formed by self-guided terawatt long-wavelength infrared laser, Nat. Photonics **13**, 41 (2019).

[38] M. Kolesik and J. V. Moloney, Nonlinear optical pulse propagation simulation: From Maxwell's to unidirectional equations, Phys. Rev. E **70**, 036604 (2004).

[39] L. Berge, S. Skupin, F. Lederer, G. Mejean, J. Yu, J. Kasparian, E. Salmon, J. P. Wolf, M. Rodriguez, L. Woste, R. Bourayou, and R. Sauerbrey, Multiple Filamentation of Terawatt Laser Pulses in Air, Phys. Rev. Lett. **92**, 225002 (2004).

[40] W. Ettoumi, J. Kasparian, and J.-P. Wolf, Laser Filamentation as a New Phase Transition Universality Class, Phys. Rev. Lett. **114**, 063903 (2015).

[41] W. Ettoumi, J. Kasparian, and J.-P. Wolf, Spin-Glass Model Governs Laser Multiple Filamentation, Phys. Rev. Lett. **115**, 033902 (2015).

[42] P. B. Corkum, Plasma Perspective on Strong Field Multiphoton Ionization, Phys. Rev. Lett. **71**, 1994 (1993).

[43] T. D. Pointon, Second-order, exact charge conservation for electromagnetic particle-in-cell simulation in complex geometry, Comput. Phys. Commun. **179**, 535 (2008).

[44] Y. Itikawa, Cross sections for electron collisions with nitrogen molecules, J. Phys. Chem. Ref. Data **35**, 31 (2006).

[45] K. S. Thorne and R. D. Blandford, *Modern Classical Physics: Optics, Fluids, Plasmas, Elasticity, Relativity, and Statistical Physics* (Princeton University Press, Princeton, NJ, 2017).

[46] J. M. Dawson, Nonlinear electron oscillations in a cold plasma, Phys. Rev. **113**, 383 (1959).

[47] O. Sakai, A. Iwai, Y. Omura, S. Iio, and T. Naito, Wave propagation in and around negative-dielectric-constant discharge plasma, Phys. Plasmas **25**, 031901 (2018).

[48] M. Okoniewski, M. Mrozowski, and M. A. Stuchly, Simple treatment of multi-term dispersion in fdtd, IEEE Microwave Guided Wave Lett. **7**, 121 (1997).

[49] E. Kretschmann, The angular dependence and the polarisation of light emitted by surface plasmons on metals due to roughness, Opt. Commun. **5**, 331 (1972).

[50] S. J. Smith and E. M. Purcell, Visible light from localized surface charges moving across a grating, Phys. Rev. **92**, 1069 (1953).

[51] R. Dahan, S. Nehemia, M. Shentcis, O. Reinhardt, Y. Adiv, X. Shi, O. Be'er, M. H. Lynch, Y. Kurman, K. Wang *et al.*, Resonant phase-matching between a light wave and a free-electron wavefunction, Nat. Phys. **16**, 1123 (2020).

[52] A. Sommerfeld, Ueber die Fortpflanzung elektrodynamischer Wellen längs eines Drahtes, Ann. Phys. **303**, 233 (1899).

[53] G. Goubau, Surface waves and their application to transmission lines, J. Appl. Phys. **21**, 1119 (1950).

[54] D. Jaisson, Simple formula for the wave number of the Goubau line, Electromagnetics **34**, 85 (2014).

[55] J. R. G. Mendonça, Electromagnetic surface wave propagation in a metallic wire and the Lambert W function, Am. J. Phys. **87**, 476 (2019).

[56] J. B. Andersen, Radiation from surface-wave antennas, Electron. Lett. **3**, 251 (1967).

[57] M. Sporer, R. Weigel, and A. Koelpin, A 24 GHz dual-polarized and robust dielectric rod antenna, IEEE Trans. Antennas Propag. **65**, 6952 (2017).

[58] K. Amini, J. Biegert, F. Calegari, A. Chacón, M. F. Ciappina, A. Dauphin, D. K. Efimov, C. F. de Morisson Faria, K. Giergiel, P. Gniewek *et al.*, Symphony on strong field approximation, Rep. Prog. Phys. **82**, 116001 (2019).

[59] S. D. Baalrud and J. Daligault, Effective Potential Theory for Transport Coefficients across Coupling Regimes, Phys. Rev. Lett. **110**, 235001 (2013).

[60] Z. Donkó, Molecular dynamics simulations of strongly coupled plasmas, J. Phys. A: Math. Theor. **42**, 214029 (2009).